RESEARCH ARTICLE

Macro-
molecular
Materials and Engineering
Open Access
www.mame-journal.de

Check for updates

3D-Printed Inherently Porous Structures with Tetrahedral Lattice Architecture: Experimental and Computational Study of Their Mechanical Behavior

*Maria A. Kuzina, Chantal M. Kurpiers, Ya-Yun Tsai, Ruth Schwaiger, Shu-Wei Chang, and Pavel Levkin**

Increasing demand in automotive, construction, and medical industries for materials with reduced weight and high mechanical durability has given rise to porous materials and composites. Materials combining nano- and microporosity and a well-defined cellular macroporous architecture offer great potential weight reduction while maintaining mechanical durability. To achieve predictable mechanical performance, it is essential to apply experimental and computational efforts to precisely describe material structure–properties relationships. This study explores polymer structures with polymerization-inherited porosity and well-defined macroporous geometry, fabricated via digital light processing (DLP) 3Dprinting. Pore size and relative density are varied by ink composition and printing parameters to track their influence on the structure stiffness. Simulated stiffness values for the base polymer correspond to the experimentally determined elastic properties, showing Young's moduli of 554–722 MPa depending on the cosolvent ratio, which confirms the structure–properties relationship. Macroporosity is introduced in the form of a 3D tetrahedral bending-dominated architecture with the resulting specific Young's moduli of 79.5 MPa cm^3 g^{-1}, comparable to foams. To merge the gap in stiffnesses, further investigation of structure–property relationships of various 3D–printed lattice architectures, as well as its application to other stereolithography methods to eliminate the negative effects from printing artifacts and resolution limit of the DLP 3D-printing, are envisioned.

1. Introduction

Polymerization-induced phase separation is a one-step process enabling control and manipulation of the polymer porous structure.[1] Due to the rapidly increasing immiscibility of the growing oligomer chains with the liquid porogen, a liquid–solid biphasic system is formed.[2] In this work, we use three terms to describe porous materials: nanoporous (pore size is up to 1 μm), microporous (pore size ranges from 1 to 10 μm), and macroporous (3D–printed pores larger than 100 μm). Subsequent removal of the liquid phase creates continuous nano- to macroporous structures without sintering or blowing agents, as it would be required for ceramics or polymer foams.[3,4]

Recently, it has been found that as the phase separation process is quickly initiated by free-radical polymerization, it is compatible with advanced fabrication methods and foremost, with stereolithography.[5] A method combining bottom-up self-assembling of nanoporous polymer via phase-separation with top-down digital

M. A. Kuzina
Institute of Biological and Chemical Systems—Functional Materials Systems (IBCS-FMS)
Karlsruhe Institute of Technology (KIT)
76344 Eggenstein-Leopoldshafen, Germany
C. M. Kurpiers
Institute for Applied Materials (IAM)
Karlsruhe Institute of Technology (KIT)
76344 Eggenstein-Leopoldshafen, Germany

C. M. Kurpiers
DMM2O – Cluster of Excellence (EXC-2082/1-390761711)
Karlsruhe Institute of Technology (KIT)
76131 Karlsruhe, Germany
Y.-Y. Tsai, S.-W. Chang
Department of Civil Engineering
National Taiwan University
10617 Taipei, Taiwan
R. Schwaiger
Institute of Energy and Climate Research—Microstructure and Properties of Materials (IEK-2)
Forschungszentrum Jülich
52425 Jülich, Germany
R. Schwaiger
Chair of Energy Engineering Materials, Faculty 5
RWTH Aachen University
52072 Aachen, Germany
S.-W. Chang
Department of Biomedical Engineering
National Taiwan University
10617 Taipei, Taiwan

light processing (DLP)[6] and two-photon polymerization[5] 3D-printing of polymer architectures was demonstrated. Based on the reported technique, structures with ordered 3D–printed architectures based on the inherently porous material could be fabricated. Despite the method's simplicity and high resolution of the printed features, a number of questions regarding the material structure–properties relationship as well as the ways of controlling the elastic response through architectural design have not yet been addressed. For such materials with a random distribution of pores, the lack of robust methods to control the microstructure and predict their mechanical behavior remains a big limitation.

Polymers with intrinsic porosity can have densities much lower than that of nonporous polymers. Porous lightweight polymers are opening perspectives for their use as construction or biomaterials.[7,8] Reported research on 3D-printing of hierarchical porous polymers includes printed via fused deposition modelling carbon nanotube/chitosan composites,[9] conductive 3D-printed TiO_2-$Ti_3C_2T_x$ heterojunction/reduced graphene oxide (rGO)/polydimethylsiloxane(PDMS) composites with the vertical porosity gradient,[10] as well as rGO@Fe_3O_4/rGO@MXene/PDMS composite materials.[11] However, reducing weight by increasing porosity is always limited by its negative effect on mechanical properties, such as reduced stiffness and fracture toughness.[12,13] By contrast, 3D-printed materials with rationally designed porous architectures are capable of achieving mechanical properties exceeding those of their bulk counterparts.[14] Lattice architectures of different geometries can exhibit superior stiffness-to-weight ratios due to the well-defined cellular architecture.[8,15–18] For certain types of lattice-based microporous or meta-biomaterials the traditional correlations between Young's moduli and strength can be different allowing the creation of functional materials with targeted mechanical properties.[19–22] The stiffness of such printed structures, for example, can be manipulated by varying the dimensions of the struts and the number of cells[23] but also through variation of the strut and node geometries by changing the printing parameters.[24] Therefore, developing new lattice-based architectures based on the precisely evaluated mechanical parameters of the base materials is envisioned.

Here, we investigated the mechanical behavior of 3D-printed inherently porous polymers combining microcompression experiments using a nanoindenter and simulation of elasticity, porosity, and stress distribution based on the Lattice Spring Model.[25–27] The effects of varying compositions and printing layer thickness on the mechanical behavior were studied both experimentally and by simulation. By conducting this survey, we provide a set of tools and perspectives for further investigation of 3D-printed phase-separation-induced porous polymers for lightweight 3D-architectured materials.

P. Levkin
Institute of Organic Chemistry (IOC)
Karlsruhe Institute of Technology (KIT)
76021 Karlsruhe, Germany
E-mail: levkin@kit.edu

Table 1. Ink compositions with the varied co-porogen ratio.

Ink 1	Ink 2	Ink 3
Samples M1-M3	Samples M4-M6	Samples M7-M9
30 wt% HEMA,	30 wt% HEMA,	30 wt% HEMA,
20 wt% EDMA,	20 wt% EDMA,	20 wt% EDMA,
40 wt% cyclohexanol,	30 wt% cyclohexanol,	20 wt% cyclohexanol,
10 wt% 1-decanol,	20 wt% 1-decanol,	30 wt% 1-decanol,
1 wt% Irgacure 819,	1 wt% Irgacure 819,	1 wt% Irgacure 819,
0.1 wt% Sudan I	0.1 wt% Sudan I	0.1 wt% Sudan I

2. Experimental Section

2.1. Ink Preparation

The monomers 2-hydroxyethyl methacrylate (HEMA, purchased from Sigma-Aldrich, Darmstadt, Germany), ethylene glycol dimethacrylate (EDMA, purchased from MERCK KGaA, Darmstadt, Germany), initiator phenylbis(2,4,6-trimethylbenzoyl)phosphine oxide (Irgacure 819,S u. K Hock GmbH, Regen, Germany), as well as two cosolvents 1-decanol and cyclohexanol (both purchased from Sigma-Aldrich, Darmstadt, Germany), were mixed, stirred, and sonicated for 30 min into a homogeneous ink. To achieve the highest resolution simultaneously with high stiffness, both a high ratio of monomers to solvents and high content of the cross-linking component is required. Based on the results of the previous study, the ratio HEMA : EDMA equal to 3 : 2 and the relative content of monomers to solvents of 50 wt% were used.[6]

The exact ink compositions are shown in **Table 1**.

To avoid aging, all inks were stored in amber glass vials at 5 °C and renewed regularly.

2.2. 3D Printing

A commercial DLP-based 3D printer Miicraft 110 Prime (Miicraft, Taiwan, working principle demonstrated in Figure S1A, Supporting Information) was used to print cylindrical pillars and complex tetrahedral architectures. All models were created in Inventor software (Autodesk Inventor, Autodesk Inc., San Rafael, USA) and imported into the printer as a .stlfile.

As changing the ink composition affects the conversion efficiency of the ink, the printing times for some of the samples were changed based on the printing quality:

Cylindrical pillars with a diameter of 500 µm (matching the flat indenter tip) and a height-to-diameter ratio of 3:1 were printed with the following printing settings:

For Ink 1 and Ink 2, power ratio and printing time of 50% and 100 s, respectively, were used.

For Ink 3, the power ratio was 50% and the printing time 150 s. The tetrahedral structures (height—4 mm, top diameter—8.7 mm) were printed using the following printing settings: a layer thickness of 50 µm, a power ratio of 50%, and a curing time of 70 s for Ink 1 and 100 s for Ink 2.

Each printing time was adjusted experimentally based on the best printing quality.

For easier handling, all objects were printed on previously functionalized microscopy glass substrates (Figure S1A, Support-
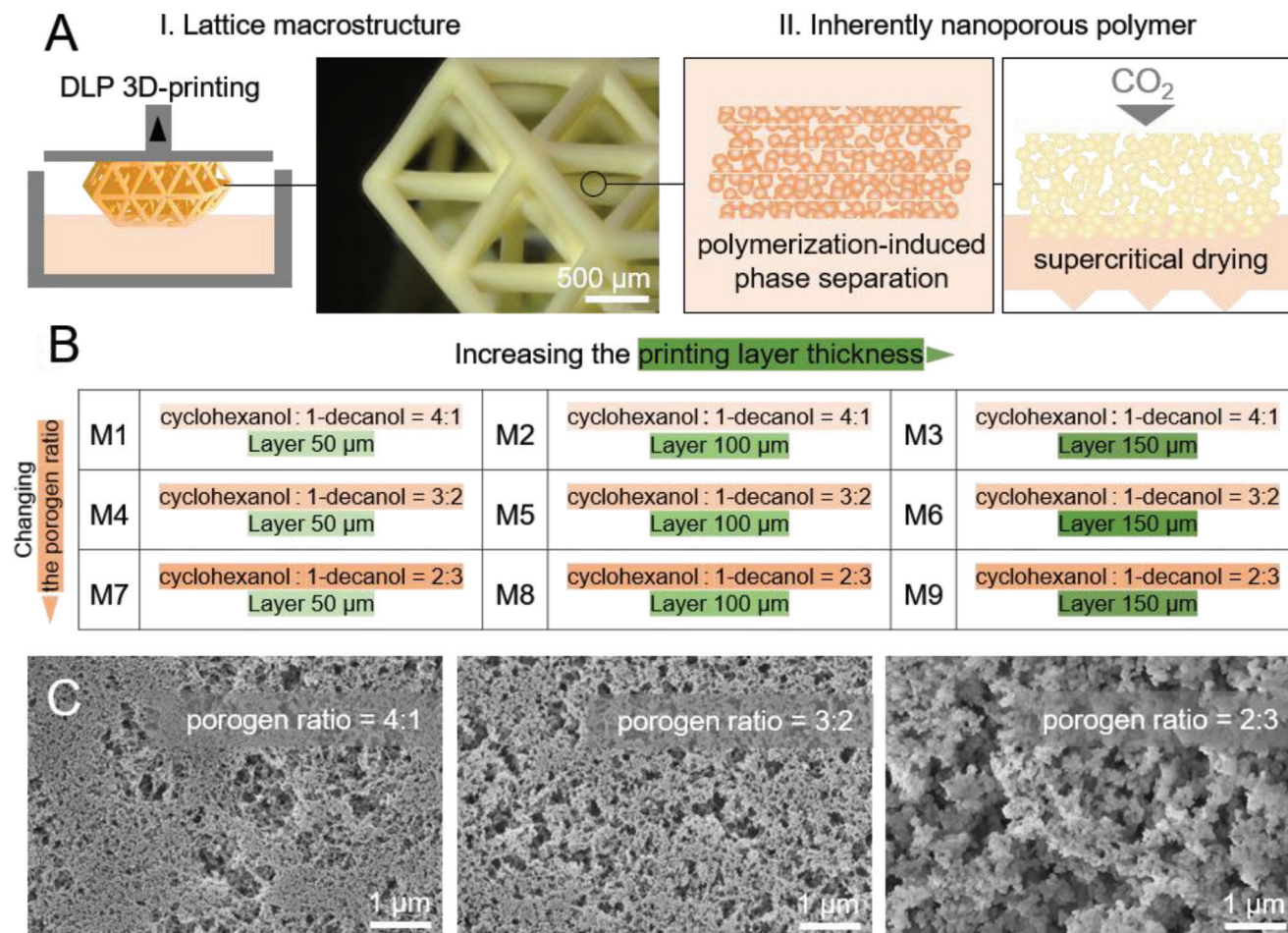
ADVANCED
SCIENCE NEWS

www.advancedsciencenews.com

Macro-
olecular
Materials and Engineering
Open Access

www.mame-journal.de

Figure 1. Fabrication of micro- and macroporous polymers via DLP 3D–printing combined with polymerization-induced phase separation. A) Fabrication scheme. B) Description of sample naming. Samples M1-M9 were printed from inks* with three different porogen ratios (cyclohexanol : 1-decanol) (rows) and various printing layer thicknesses increasing from 50 to 150 μm (columns). C) Microscopy images show changing porosity and the size of particle agglomerates with porogen ratio changing from 4:1 to 2:3. *Detailed composition of each ink is given in Table 1.

ing Information). The samples, i.e., printed structures on the glass substrates, were put in acetone and dried vertically in the critical point dryer (Figure S1B, Supporting Information).

2.3. Substrate Functionalization

Microscopy cover glasses of 22×22 mm size and 170 ± 5 μm thickness (purchased from Paul Marienfeld GmbH & Co KG, Lauda-Königshofen, Germany) were cleaned by isopropanol and ozone cleaner for 10 min. Then, the substrates were submerged overnight in a solution of 25 mL of absolute ethanol mixed with 1 mL of 3-(trimethoxysilyl)propyl methacrylate (purchased from Alfa Aesar). Finally, the slides were rinsed with ethanol and blow-dried by an air gun.

2.4. Samples Drying

After detaching from the printing platform, the samples on the glass substrates were soaked in acetone for 24 h. To remove the

residual solvent, the samples on the substrates were dried using an Automated Critical Point Dryer (Leica EM CPD030, Germany).

2.5. Microstructural Characterization

The printed structures were characterized using a scanning electron microscope (SEM, Zeiss LEO 1530) at an operating voltage of 5 kV with an InLens detector. Prior to the SEM measurements, the samples were coated with a 10 nm thick carbon layer (EM ACE 600, Leica Microsystems GmbH, Germany).

2.6. Particle Agglomerate Size Analysis

To estimate the average size of particle agglomerates of the porous polymer, the size distribution was estimated by the calculation of Feret's diameter. Boundaries of the agglomerates were manually delineated in the ImageJ software.[28] From the measured diameters, the average size and standard deviation were calculated. The size distribution was visualized by the normal distribution curve.
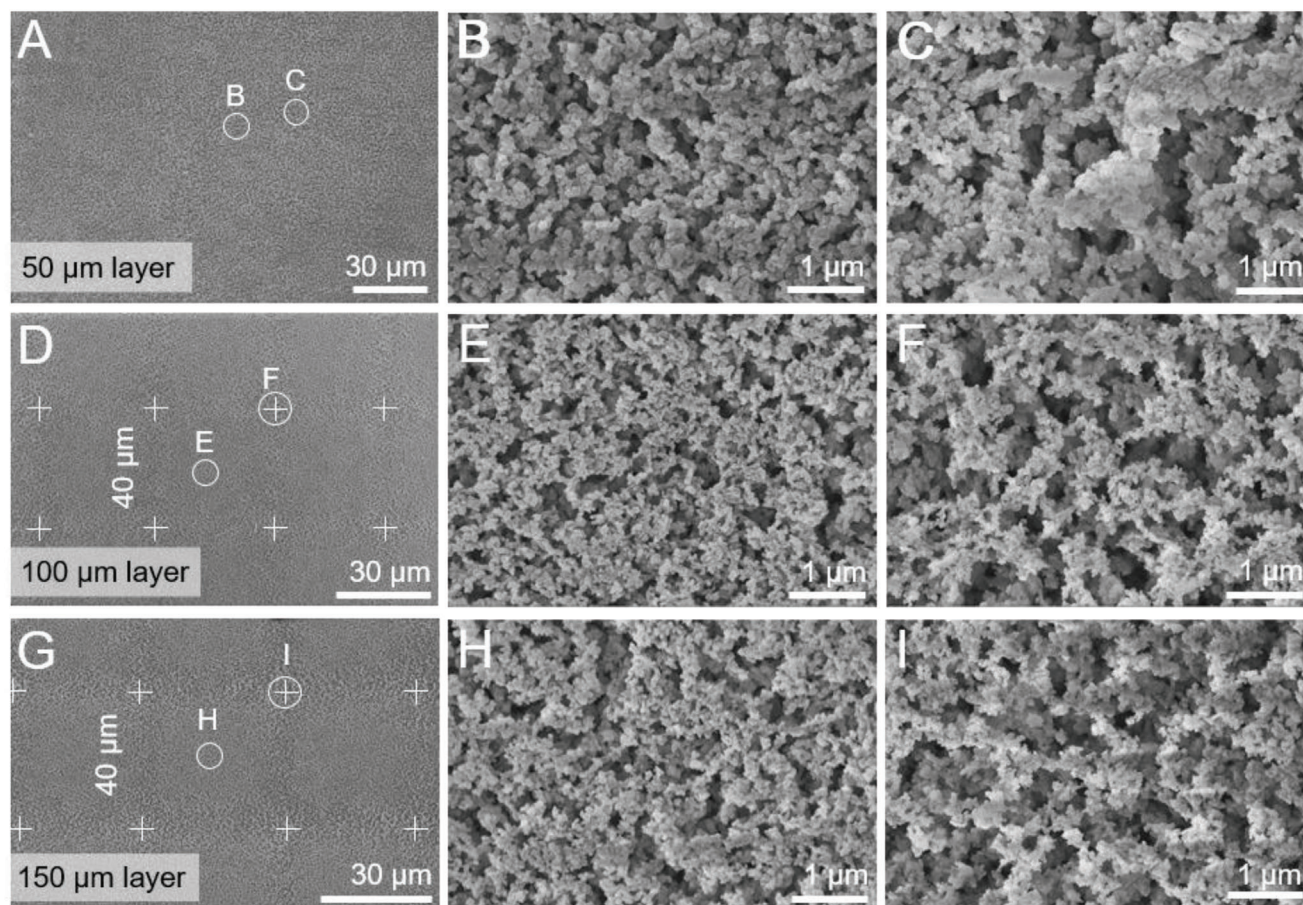
Figure 2. Surface morphology of samples M7-M9 after drying step (porogen ratio cyclohexanol : 1-decanol equals 2:3, the printing layer thickness is varied): A–C) 50 μm printing layer, sample M7. D,F) 100 μm printing layer, sample M8, G–I) 150 μm printing layer, sample M9. For the 100 μm D) and 150 μm G) printing layers, a "voxel grid" is visible, which is a printing artifact of DMD mirrors B,E,H).

2.7. Morphology and Elasticity Modeling by the Lattice Spring Model

Elasticity modeling was performed by the lattice spring model (LSM), which is a coarse-grained particle-based model, adopted from the previous works.[29,30] For simulations, a 2D LSM with hexagonal packing particles and a triangular spring network was used, in which each particle binds with its first nearest neighbors through harmonic springs. All the simulations were performed by the open-source software LAMMPS (https://www.lammps.org).[31] The 2D simulation models were constructed from 35 SEM images (three for the sample M6 and four for others). First, each SEM image was reproduced 15 times by random crop. The cropped images were transformed into discrete particle models by img2particle software.[30,32] Two edges at the left and right were added to the models to grip the samples during the uniaxial tensile tests. Finally, a uniaxial tensile load was applied horizontally based on the computational framework described in Libonati et al.[26]

2.8. Microcompression Testing

To determine the mechanical properties depending on porosity and layer thickness in the printing process, compression tests using an Agilent Technologies nanoindenter system (G200 XP, Agilent Technologies Inc., Santa Clara, USA) were carried out. For each parameter set, three pillars were tested by compressing them at a displacement rate of 100 nm s^{-1} with a diamond flat punch of 600 μm diameter until the maximum force of the indenter ($\approx$500 mN) was reached. Then, the load was removed at the same rate. With the mean value of the diameter and height of the pillars, which were measured using a digital microscope (VHX-7000, Keyence Corporation, Osaka, Japan), stress and strain were calculated. Young´s modulus was determined from the slope of the unloading curve.

The tetrahedral lattices were tested with a continuous stiffness measurementperformed by using the indenter (Anton Paar, Switzerland) equipped with a custom-made Al flat punch with a diameter of 5 mm. The compression tests were conducted with
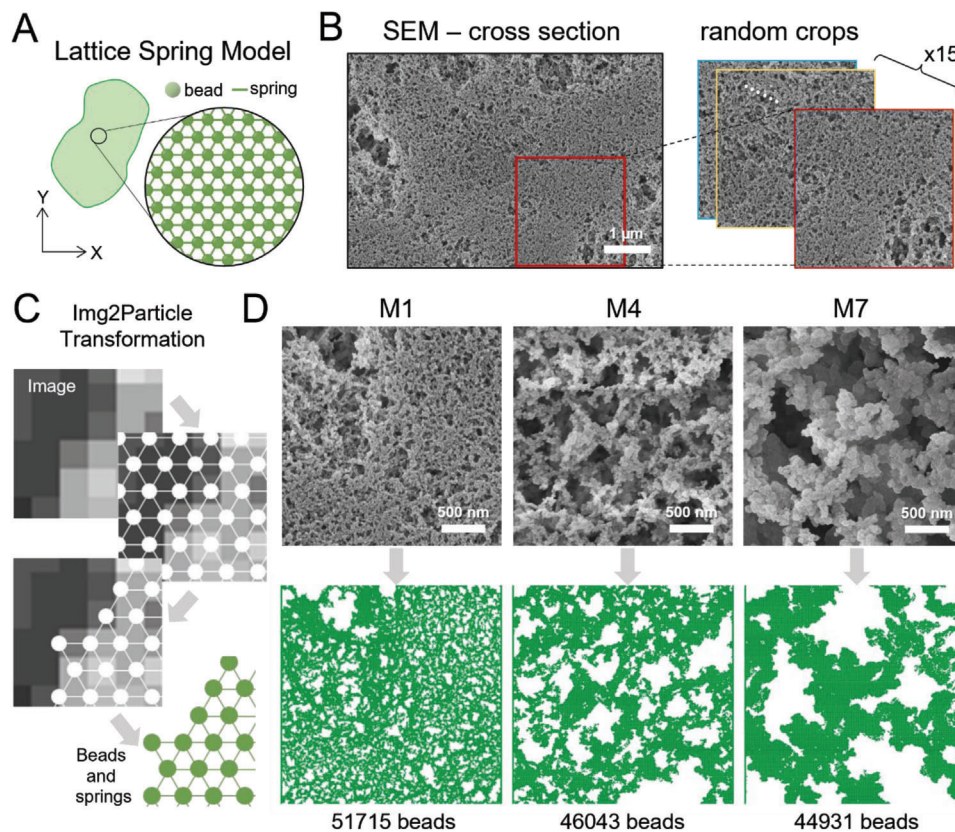
Figure 3. Preparing SEM images for the computational analysis. A) Illustration of the 2D triangular LSM. B) An SEM image of the top surface of the pillar is cropped at a random location 15 times. C) Illustration of the image-particle conversion tool, Img2Particle.[32] D) Three examples of the converted bead models.

a loading rate of 0.5 N min⁻¹ until reaching the maximum force of 6 N. Stress and strain were estimated based on the area of the top layer of the tetrahedral structure and the height before loading (Figure 6A).

3. Results and Discussion

To create structures with photopolymerization-induced porosity, DLP-based 3D-printing was used. The phase separation of polymer particles from a porogen solvent is crucial for creating and manipulating porosity, making it an essential factor in the process. To achieve this, hydrophilic monomer HEMA and crosslinker EDMA were selected. The phase separation process was triggered by a mixture of porogenic solvents, cyclohexanol, and 1-decanol, resulting in a biphasic system. To investigate the mechanical properties of the porous base material, pillars of 500 µm diameter and 1.5 mm height (Figure S1, Supporting Information) were printed. The effect of the printing process on the porous structure, and thus the mechanical behavior, were evaluated for the series of samples with two parameters being varied: 1) the ratio between two coporogens 1-decanol and cyclohexanol, and 2) the thickness of one printing layer, which amounted to nine final compositions (later referred as samples M1-M9, see **Figure 1**B). The exact porogen fractions in each ink are shown in Table 1.

With increasing the fraction of 1-decanol in the porogenic mixture from 25 to 60 wt%, the surface morphology changes from the dense network of small granules and pores below 1 µm (Figure 1B, left) to agglomerates of big particles and large interconnected pores up to 10 µm (Figure 1B, right). To evaluate the particle agglomerates, given their arbitrary shape, the mean Feret's diameter was measured as the average distance between the two parallel planes restricting each agglomerate perpendicular to their direction. Mean values of Feret's diameter for the samples M1, M4, and M7, amounted to 27 ± 11, 37 ± 13, and 83 ± 19 nm, accordingly, showing the agglomeration of smaller polymer globules into larger particles for larger fractions of 1-decanol in the coporogen mixture (Figure S2A, Supporting Information).

The thickness of the printing layer has also affected the morphology. Increasing layer thicknesses from 50 to 150 µm caused an increase in inhomogeneity of the particle agglomerates and pore sizes (**Figure 2**). The pattern in the form of the grid was observed for the larger printing layers with the size of one grid element ≈40 µm, which corresponds to the "voxel" size of the printer. This can be explained by the effect of scattering the projected light in the larger volume for thicker printing layers causing lower polymerization rates on the edges of the voxel. Lower irradiation intensity on the edges of the "voxels" affected the particle size as well, leading to lower average size and narrower size distribution of agglomerates (Figure S2B, Support-
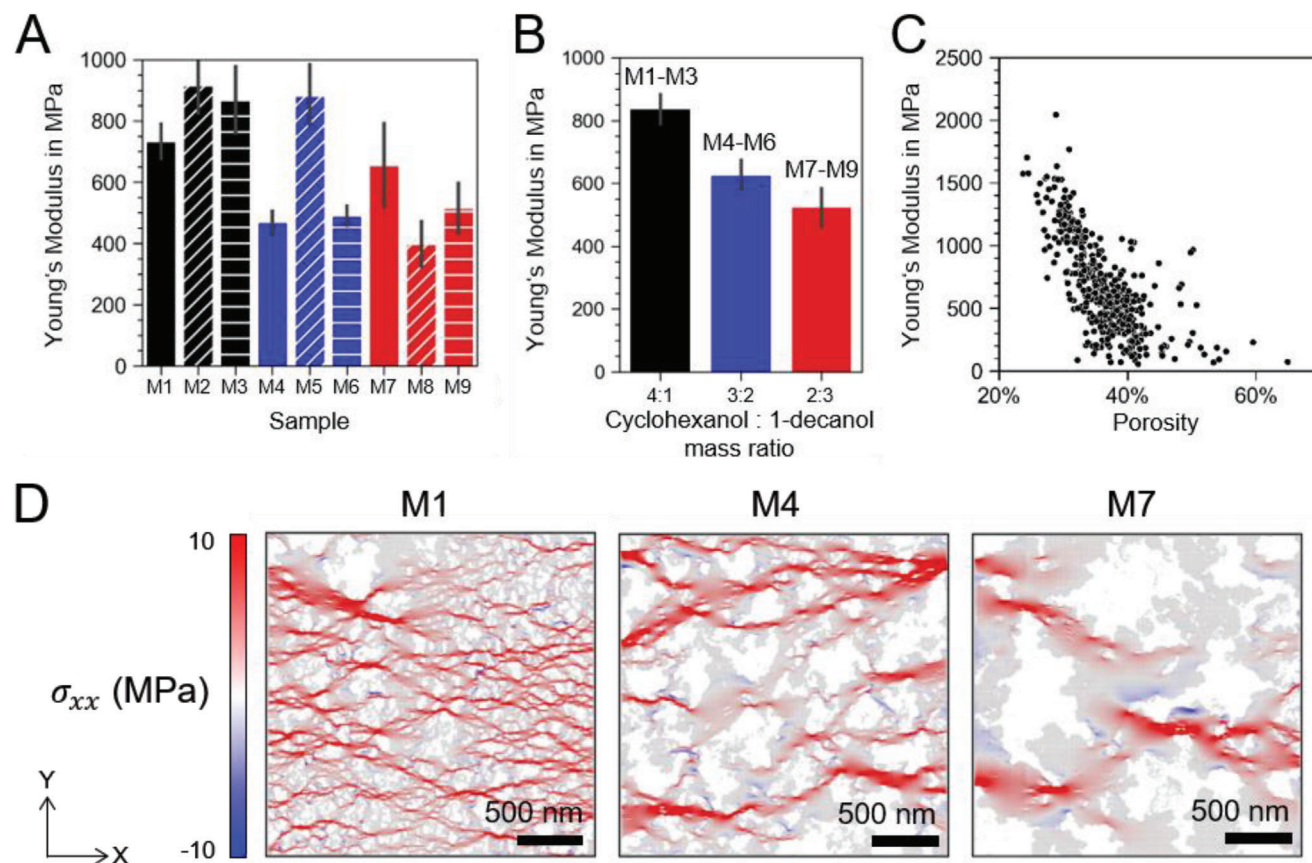
**ADVANCED
SCIENCE NEWS**

www.advancedsciencenews.com

{M} acro-
olecular
Materials and Engineering
Open Access

www.mame-journal.de

Figure 4. Computational data on mechanical and topological parameters. A) Young's modulus of simulated models from M1 to M9 with 95% confidence interval error bars. The black, blue, and red colors denote the porogen ratio (cyclohexanol : 1-decanol) of 4:1, 3:2, and 2:3, respectively. Different textures of the bars represent different printing thicknesses: blank for 50 μm, diagonal hatching for 100 μm, and horizontal hatching for 150 μm. B) Young's modulus decreases with increasing 1-decanol fraction in the porogen ratio, as the averaged values for the series M1-M3, M4-M6, M7-M9 show. C) Scatter plot of porosity values calculated from converted microscopy images versus Young's modulus for all 482 simulated data points. D) Three examples of stress distribution at the strain of 0.075% in the X-direction. The blue-white-red color bar represents the local compressive and tensile stress in the X-direction.

ing Information). Same artifact patterns have been observed for the inks with 1-cyclohexanol : 1-decanol ratio of 4:1 (Figure S2C, Supporting Information) and 3:2 (Figure S2D, Supporting Information) with larger printing layers as well. Additionally, the increased thickness of the printing layer caused a significant decrease in the z-resolution from almost unnoticeable borders of the layer for the 50 μm layer (Figure S2E, Supporting Information) to the conic shape and unstable thickness of layers for the 100 and 150 μm layer (Figure S2G, Supporting Information).

To simulate elasticity, microscopy images were evaluated using various models, including the Lattice Spring Model (LSM), the coarse-grained model, the spring network, and the bead-spring models. LSMs have been previously adopted in many studies on the mechanics of bio-inspired or 3D-printed materials as straightforward and effective techniques.[26,30,33–35] As illustrated in **Figure 3**A, the idea of LSMs is representing a solid by a bead-spring network, in which each bead represents a small portion of the materials interacting with other portions via harmonic springs. SEM images of the top surface of the pillar have been randomly cropped (Figure 3B) and transformed into discrete particle models by an image-to-particle conversion tool, Img2Particle

(Figure 3C).[32] The results of the converted LSMs are given in Figure 3D for samples M1, M4, and M7.

Young's modulus values for 525 simulation models were calculated based on the slopes of the stress–strain curves from 0.01% to 0.1% strain after applying horizontally to the bead model a uniaxial tensile load. All the stress–strain curves are provided in Figures S3–S5 (Supporting Information). Since some of the clusters on the crops were poorly interconnected, and the resulting Young's moduli were significantly lower, those with Young's modulus of less than 50 MPa were excluded. Therefore, the number of valid data points is 482. The average Young's modulus from M1 to M9 has been compared as shown in **Figure 4**A,B, respectively. Simulation results showed decreasing Young's modulus with an increasing 1-decanol fraction in the co-porogen mixture. Figure 4C depicts Young's modulus against porosity and shows an inversely proportional relationship. Likewise, Young's modulus is proportional to the volume density (Figure S7, Supporting Information). Other than the key factor, porosity (or volume density calculated as 1–porosity), the topology of the porous structures also plays an important role in stiffness. Additionally, we have developed an approach to analyzing the topological features (Figure S8, Supporting Information). Figure 4D demonstrates
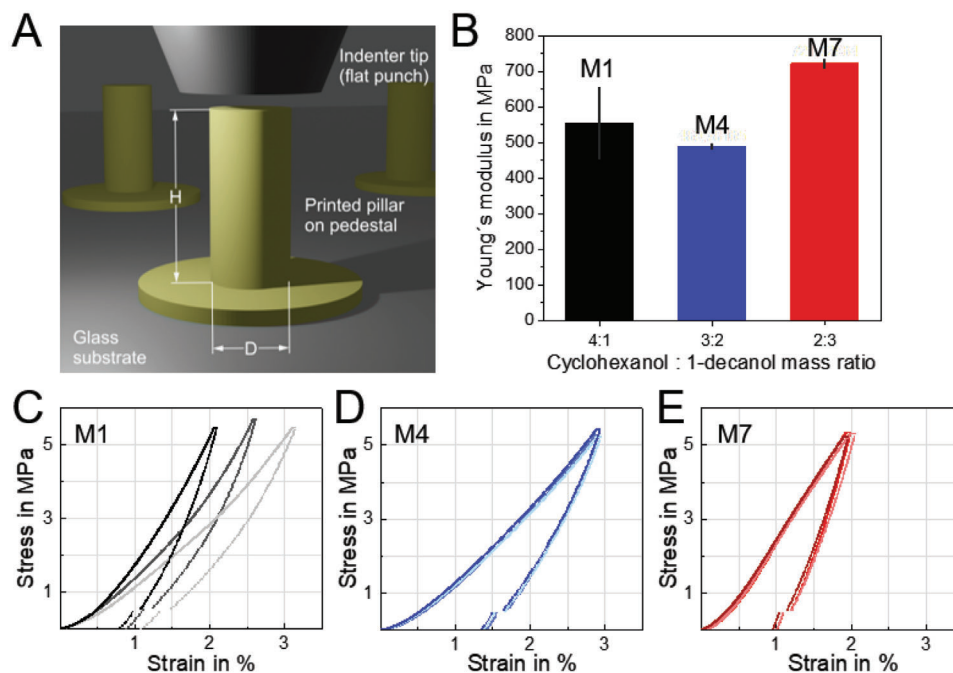
**ADVANCED
SCIENCE NEWS**

www.advancedsciencenews.com

acro-
olecular

Materials and Engineering

www.mame-journal.de

Figure 5. Compression tests for 3D-printed pillars. A) A scheme of the experimental setup of pillar compression with a flat punch. Pillars with diameter *D* and height *H* were printed on a glass substrate and a thin pedestal. B) Averaged Young´s modulus with standard deviation for samples M1, M4, and M7 (cyclohexanol : 1-decanol mass ratio equal to 4:1, 3:2, and 2:3, respectively) in MPa. C–E) Stress–strain curves of pillar compression tests in the nanoindenter of M1, M4, and M7. For each condition, three pillars were tested. Error bars in (B) are standard deviations.

the load transfer through the struts by showing the stress distributions of M1, M4, and M7, in which M1 has significantly more load transfer paths.

Based on the force and displacement data obtained from micro-compression tests (schematically shown in **Figure 5**A), the stress and strain curves as well as the elastic moduli of the different materials were determined (Figure 5B,E). Young´s modulus was determined as the slope of the unloading curve. The stress–strain curves in Figure 5C–E show the behaviors of three different material compositions with cyclohexanol : 1-decanol ratio of 4:1, 3:2, and 2:3, respectively. The samples printed with the smallest layer thickness of 50 μm, i.e., samples M1, M4, and M7 (see Figure 1B and Table 1), were selected due to the higher z-printing resolution (cf., Figure S2E, S2F, Supporting Information). With increasing strain, the slope of the loading curves increases, while the curves also show permanent deformation of the pillars after unloading. This behavior may indicate densification of the materials or a change in the cross-section of the pillars. The mechanical behavior was very reproducible for samples M4 and M7, whereas the tests of M1 show a significant variation in the slope of the curves. This is reflected in the values of Young´s modulus, shown in Figure 5B. From M1 to M4 a decrease of Young's modulus from 554 to 490 MPa was measured with M1 showing the highest standard deviation of 100 MPa. The modulus then increases to 722 MPa for M7. These results agree well with the trends revealed by simulation (Figure 4A), showing lower stiffness for samples with a lower fraction of 1-decanol in the co-porogen mixture (M1 and M4) and an increase in stiffness for the composition with the largest 1-decanol fraction (M7). This observation is in contrast to the reported trend of

decreasing stiffness with increasing porosity.[36,37] The variation in the mechanical performance of M1 pillars can be assigned to a more heterogeneous pore distribution (see Figure 3C). The M1 material reveals finer cell walls, resulting in critical sites for instabilities such as buckling or brittle fracture at the thinnest cell walls.[38] Samples M4 and M7 show larger pores with a rather homogeneous distribution. As stated above, with increasing 1-decanol fraction in the co-porogen mixture, the agglomeration to bigger particles was observed. Thus, the higher stiffness of M7 can be attributed to thicker cell walls between pores, as shown in Figure 4D. The mechanical properties are in good agreement with the simulation results (Figure 4A) and reveal increasing stiffness upon an increase of 1-decanol fraction in the co-porogen mixture from 40 wt% (M4) to 60 wt% (M7). Young´s moduli over the density of M1 and M4 pillars are shown in the Ashby plot in Figure 7. It is worth mentioning that since layer-by-layer printing was used to print all the structures for mechanical characterization in the current study, Young´s modulus values are influenced by overlapping layers and the distribution of porosity gradients within and between the layers. Therefore, the stiffness values of the nonlayered base material with the same composition can differ from the presented values for the DLP 3D-printed material.

After the characterization of the porous materials, 3D lattice architectures were fabricated with the same technique (**Figure 6**). 3D stretching-dominated tetrahedral architectures made of M1 and M4 materials were printed at the resolution limit of the technique resulting in millimeter-sized lattice structures. The diameter *D* at the top surface layer was 7.7 mm for M1 and 7.9 mm for M4 and the height *H* was 3 mm for M1 and 3.6 mm for M4

ADVANCED
SCIENCE NEWS
www.advancedsciencenews.com

{M} acro-
olecular
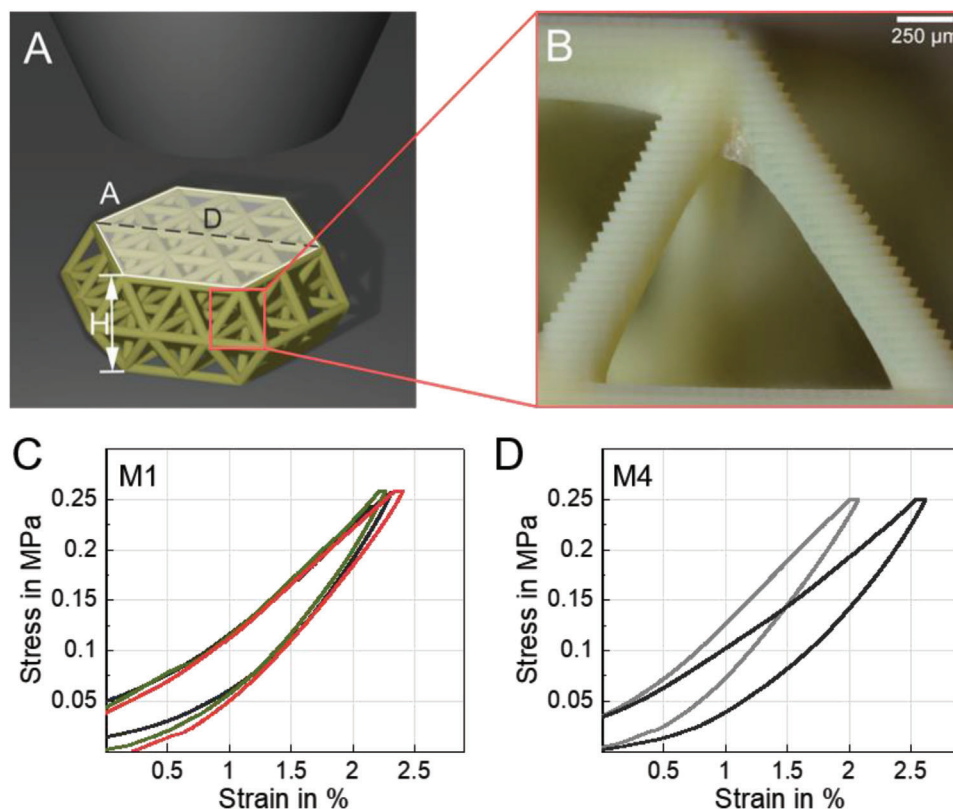Materials and Engineering
Open Access

www.mame-journal.de

Figure 6. Compression tests of 3D-printed tetrahedral structures with intrinsic micro-porosity. A) Schematic of compression test of a tetrahedral structure using a flat punch. Stress and strain were determined using the top area *A* and the height *H*, respectively, before the test. B) The beams of the tetrahedral structure had diameters of 300–370 µm and step sizes of 50 µm as determined by light microscopy. C) Representative stress–strain curves of tetrahedral structures under a compressive load of M1 material and D) M4 material.

(Figure 6A). Beam elements with diameters in the range of 300–370 µm show steps of 50 µm in the z-direction due to a layer-by-layer printing principle (Figure 6B).

Compressive stress–strain curves of the lattice structures were determined with the top surface area and height shown in Figure 6A. Representative stress–strain curves for the two materials tested are shown in Figure 6C,D. Since we are using the area of the top layer of the structures to estimate the stress, the stress values shown in Figure 6 represent an upper bound. To account for the misalignment of tip and sample or roughness at the surface, which shows as the flat region at the beginning of the curves, the curves were shifted on the *x*-axis. The elastic modulus of the porous architectures was calculated using the slope of the unloading curves yielding a mean value of 17.6 ± 2.3 MPa for M1 (mean value of ten samples) and 14.0 ± 0.5 MPa for M4 (mean value of two samples). The compression tests show reproducible deformation behavior, although manufacturing defects due to printing at the resolution limit are possible and may attribute to variations in the mechanical behavior. By combining the microporosity of the polymeric material with the macroporosity of the 3D architecture, a further density reduction was achieved. The density of the polymer M1 is 0.82 ± 0.02 g cm^{-3} with a porosity of 35%. Together with the relative density of the tetrahedral architecture of around 27%, this results in a specific stiffness of the porous tetrahedral structures of 79.5 MPa cm^3 g^{-1}. M4 tetrahedral structures reveal a density of 0.75 ± 0.04 g cm^{-3}

with a porosity of 37.9 % and therefore a specific stiffness of 69.1 MPa cm^3 g^{-1}. Thus, the hierarchical structure of porous base material and 3D lattice architecture reduces the density further while maintaining stiffness, that can be allocated to foam materials space in the Ashby plot shown as M1 tetrahedral and M4 tetrahedral in **Figure 7**. While the porous tetrahedral structures do not outperform foam materials, they exhibit advantages due to the versatile 3D architectures made possible by the 3D printing process. Thus, by adjusting microporosity through chemical variation and macroporosity through flexible 3D design, our approach expands the applicability of porous materials. Due to the high surface area created by the combination of micro- and macroporosity, a variety of applications in the field of cell growth[6] or catalysis[36] appear promising.

4. Conclusion

In this study, we successfully manufactured stiff and lightweight polymer structures with polymerization-inherited porosity and well-defined geometry. Microscopic images of the sample surfaces were used to develop a material model for simulating mechanical properties, which we compared with the results of experimental microcompression tests. The compression tests of pillars in a nanoindenter showed Young's moduli of 554, 490, and 722 MPa, depending on the cyclohexanol:1-decanol ratio, and these values were consistent with the simulated results. Our ap-
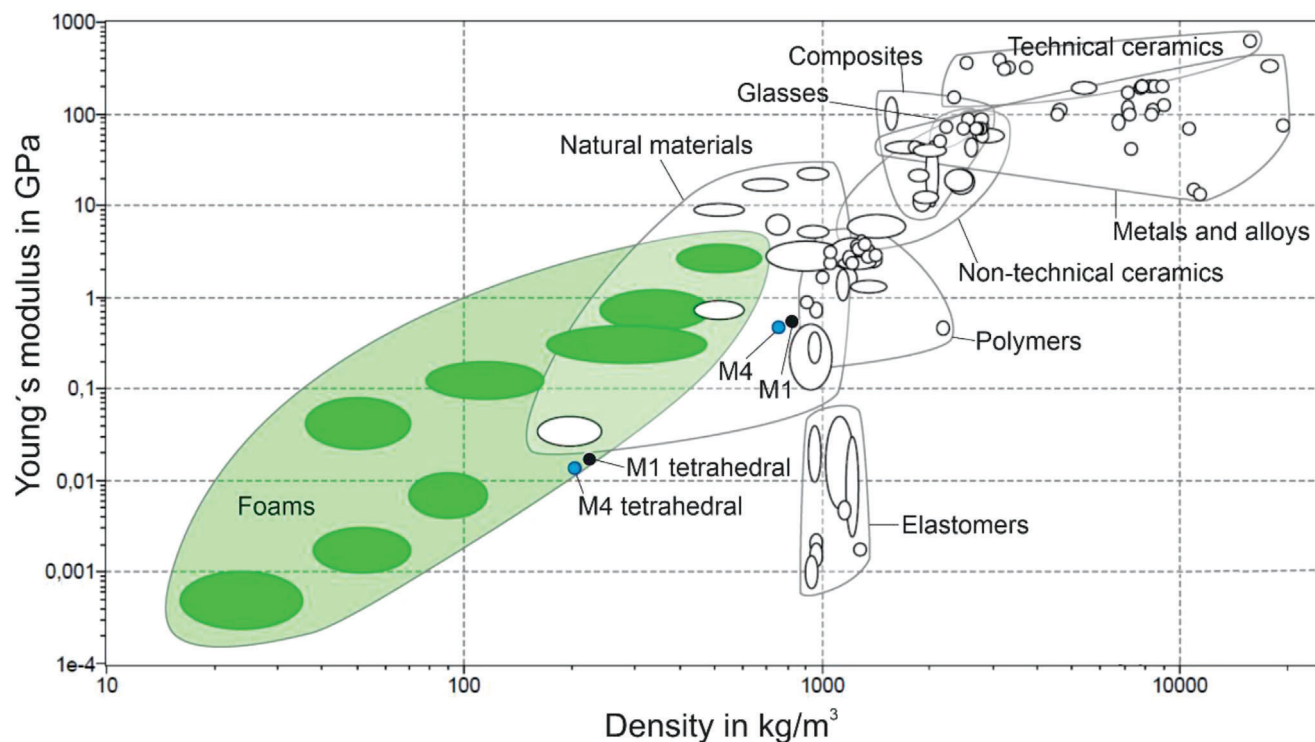
Figure 7. Young´s modulus versus density materials property chart comparing porous materials of this work with common material classes.[39] Black dots mark M1 pillars and M1 tetrahedral structures, blue dots mark M4 pillars and M4 tetrahedral structures.

proach offers the advantages of 3D-printed porous materials, including tuneable porosity, arbitrary choice of geometry, and the possibility to simulate mechanical behavior.

We also investigated the limitations and prospects of our study. The mechanical characterization of the macroporous tetrahedral lattice structures showed a specific Young's modulus of 79.5 MPa cm^3 g^{-1}, which is comparable to foam materials, as well as in the same range with other recently reported 3D-printed porous polymer materials.[9,40] However, the decrease in stiffness for macroporous structures was due to the fractures of intricate structural elements, printing at the resolution limit of the DLP method, and the drying process. We also observed other DLP printing-related artifacts, such as recessed base layers, gradient porosity within the layer and on the interfaces, and detachment of the printing layers on the edges of the structure.

Despite these limitations, we believe that our method offers promising prospects for investigating structure–property relationships of various 3D-printed lattice architectures and the base porous material. Furthermore, the application of this approach to other stereolithography methods can eliminate the influence of DLP-printing method-related artifacts.

Supporting Information

Supporting Information is available from the Wiley Online Library or from the author.

Acknowledgements

Conflict of Interest

The authors declare no conflict of interest.

Data Availability Statement

The data that support the findings of this study are available from the corresponding author upon reasonable request.

Keywords

[1] Q. Tran-Cong-Miyata, H. Nakanishi, *Polym. Int.* **2017**, *66*, 213.
[2] S. C. Leguizamon, J. Powers, J. Ahn, S. Dickens, S. Lee, B. H. Jones, *Macromolecules* **2021**, *54*, 7796.
[3] Y. Chen, N. Wang, O. Ola, Y. Xia, Y. Zhu, *Mater. Sci. Eng. R* **2021**, *143*, 100589.
[4] F. L. Jin, M. Zhao, M. Park, S. J. Park, *Polymers* **2019**, *11*, 953.
[5] F. Mayer, D. Ryklin, I. Wacker, R. Curticean, M. Čalkovský, A. Niemeyer, Z. Dong, P. A. Levkin, D. Gerthsen, R. R. Schröder, M. Wegener, *Adv. Mater.* **2020**, *32*, 2002044.

[6] Z. Dong, H. Cui, H. Zhang, F. Wang, X. Zhan, F. Mayer, B. Nestler, M. Wegener, P. A. Levkin, *Nat. Commun.* **2021**, *12*, 247.

[7] J. Göken, N. Saba, *Acta Phys. Pol. A* **2020**, *138*, 844.

[8] E. Truszkiewicz, A. Thalhamer, M. Rossegger, M. Vetter, G. Meier, E. Rossegger, P. Fuchs, S. Schlögl, M. Berer, *J. Appl. Polym. Sci.* **2021**, *139*, 51618.

[9] X. Pei, M. Zhao, R. Li, H. Lu, R. Yu, Z. Xu, D. Li, Y. Tang, W. Xing, *Composites, Part A* **2021**, *145*, 106363.

[10] G. Liu, R. Yu, D. Liu, Y. Xia, X. Pei, W. Wang, C. Min, S. Liu, R. Shao, Z. Xu, *Composites, Part A* **2022**, *160*, 107058.

[11] X. Pei, G. Liu, H. Shi, R. Yu, S. Wang, S. Liu, C. Min, J. Song, R. Shao, Z. Xu, *Compos. Sci. Technol.* **2023**, *233*, 109909.

[12] D. Liu, B. Savija, G. E. Smith, P. E. J. Flewitt, T. Lowe, E. Schlangen, *Int. J. Fract.* **2017**, *205*, 57.

[13] E. Chen, S. Luan, S. Gaitanaros, *Extreme Mech. Lett.* **2022**, *51*, 101598.

[14] R. Schwaiger, L. R. Meza, X. Li, *MRS Bull.* **2019**, *44*, 758.

[15] O. Eren, H. K. Sezer, N. Yalçın, *J. Manuf. Processes* **2022**, *75*, 1175.

[16] J. Bauer, L. R. Meza, T. A. Schaedler, R. Schwaiger, X. Zheng, L. Valdevit, *Adv. Mater.* **2017**, *29*, 1701850.

[17] X. Zheng, H. Lee, T. H. Weisgraber, M. Shusteff, J. Deotte, E. B. Duoss, J. D. Kuntz, M. M. Biener, Q.i Ge, J. A. Jackson, S. O. Kucheyev, N. X. Fang, C. M. Spadaccini, *Science* **2014**, *344*, 1373.

[18] M. Kadic, G. W. Milton, M. van Hecke, M. Wegener, *Nat. Rev. Phys.* **2019**, *1*, 198.

[19] A. Arjunan, A. Baroutaji, A. S. Praveen, J. Robinson, C. Wang, in *Encyclopedia of Smart Materials* (Ed: A. G. Olabi), Elsevier, Oxford **2020**, p. 86.

[20] H. Ma, C. Feng, J. Chang, C. Wu, *Acta Biomater.* **2018**, *79*, 37.

[21] F. S. L. Bobbert, S. Janbaz, A. A. Zadpoor, *J. Mater. Chem. B* **2018**, *6*, 3449.

[22] R. Hedayati, A. M. Leeflang, A. A. Zadpoor, *Appl. Phys. Lett.* **2017**, *110*, 091905.

[23] Z. Jia, F. Liu, X. Jiang, L. Wang, *J. Appl. Phys.* **2020**, *127*, 150901.

[24] C. M. Kurpiers, S. Hengsbach, R. Schwaiger, *MRS Adv.* **2021**, *6*, 507.

[25] G. A. Buxton, C. M. Care, D. J. Cleaver, *Model. Simul. Mater. Sci. Eng.* **2001**, *9*, 485.

[26] F. Libonati, V. Cipriano, L. Vergani, M. J. Buehler, *ACS Biomater. Sci. Eng.* **2017**, *3*, 3236.

[27] H. Chen, E. Lin, Y. Liu, *Int. J. Solids Struct.* **2014**, *51*, 1819.

[28] C. A. Schneider, W. S. Rasband, K. W. Eliceiri, *Nat. Methods* **2012**, *9*, 671.

[29] A. Ghimire, Y. Y. Tsai, P. Y. Chen, S. W. Chang, *Composites, Part B* **2021**, *215*, 108754.

[30] Y. Chiang, C. C. Tung, X. D. Lin, P. Y. Chen, C. S. Chen, S. W. Chang, *Compos. Struct.* **2021**, *262*, 113349.

[31] A. P. Thompson, H. M. Aktulga, R. Berger, D. S. Bolintineanu, W. M. Brown, P. S. Crozier, P. J. In 'T Veld, A. Kohlmeyer, S. G. Moore, T. D. Nguyen, R. Shan, M. J. Stevens, J. Tranchida, C. Trott, S. J. Plimpton, *Comput. Phys. Commun.* **2022**, *271*, 108171.

[32] Y. Chiang, T. W. Chiu, S. W. Chang, *Front. Mater.* **2022**, *8*, 803875.

[33] Y. Kim, Y. Kim, F. Libonati, S. Ryu, *Composites, Part B* **2019**, *167*, 736.

[34] Y. Y. Tsai, Y. Chiang, J. L. Buford, M. L. Tsai, H. C. Chen, S. W. Chang, *ACS Biomater. Sci. Eng.* **2021**.

[35] A. Ghimire, Y. Y. Tsai, P. Y. Chen, S. W. Chang, *Composites, Part B* **2021**, *215*, 108754.

[36] M. F. Ashby, *Philos. Trans. A: Math. Phys. Eng. Sci.* **2006**, *364*, 15.

[37] A. S. P. Lin, T. H. Barrows, S. H. Cartmell, R. E. Guldberg, *Biomaterials* **2003**, *24*, 481.

[38] G. Subhash, Q. Liu, X. L. Gao, *Int. J. Impact Eng.* **2006**, *32*, 1113.

[39] Ansys Granta EduPack | Software for Materials Education https://www.ansys.com/products/materials/granta-edupack (accessed: **2023**).

[40] V. A. Bobrin, Y. Yao, X. Shi, Y. Xiu, J. Zhang, N. Corrigan, C. Boyer, *Nat. Commun.* **2022**, *13*, 3577.